Structural and electrical properties of nanocolumnar W-Mo thin films with a Janus-like structure

Houssem Boukhalfa[1], Valérie Potin[1*] and Nicolas Martin[2]

[1]Laboratoire Interdisciplinaire Carnot de Bourgogne (ICB), UMR 6303 CNRS Université Bourgogne Franche-Comté, 9, Avenue Alain Savary, BP 47 870, F-21078 Dijon Cedex, France

[2]Institut FEMTO-ST, UMR 6174 CNRS Université Bourgogne Franche-Comté, 15B, Avenue des montboucons, 25030 Besançon Cedex, France

[*] Corresponding author: valerie.potin@ubourgogne.fr

Abstract

A Janus-like structure is obtained in W-Mo thin films with a clear separation between both metals. Thin films are deposited on glass and silicon substrates by magnetron co-sputtering using glancing angle deposition technique with two tilted targets (oblique angle $\alpha = 80°$). Films (two thickness series of 300 nm and 1 µm) are prepared with the same pressure (0.33 Pa) and tungsten target current (I_W = 140 mA) but with various molybdenum target currents (from 10 to 200 mA). The effect of Mo target current and thickness on the films microstructure and electrical response is investigated using scanning and transmission electron microscopy, X-ray diffraction and van der Pauw method. Porous and columnar W-Mo thin films with inclined columns are obtained due to the shadowing effect. Playing on the Mo target current allows controlling the architecture of the films until obtaining columns perpendicular to the substrate surface and equivalent W and Mo atomic concentrations. X-ray diffraction shows a significant thickness effect on the films microstructure with dominance of α or β phases of W for 1 µm or 300 nm, respectively. From transmission electron microscopy, W and Mo are pointed out in distinct sides of the columns and a finer structural analysis supports the clear separation between W and Mo. This two components design is repeated for all columns in the film proving that W-Mo thin films exhibit a Janus-like structure.

Keywords

Thin films, co-sputtering, columns, Janus structure, electrical resistivity, anisotropy

1. Introduction

In a few decades, a new particle design has been discovered and called Janus particle in reference to the two-faced Roman God of the same name. These objects composed of two or more elements in the same particle present some distinct physical and chemical properties. Such a Janus structure was first introduced by Casagrande et al. [1] who described spherical particle formed by two different hydrophilic and hydrophobic hemispheres. This kind of structures was highlighted after the Nobel price obtained by de Gennes in 1992 [2] who described asymmetric colloidal particle presenting anisotropic physical and/or chemical properties. Janus structures have demonstrated enhanced magnetic [3-4], electrical, catalytic [5] and optical [6] properties. New superstructural materials have been developed based on Janus particle with various shapes and compositions [7]. They have demonstrated great potential in numerous applications including biological applications [8], interfacial stabilizers [7], micro- and nano-motors [9].

Janus particle can be divided into three categories: polymeric, inorganic and polymeric-inorganic composition [10]. The polymeric Janus particles are produced with different materials such as polystyrene (PS) and poly (methyl methacrylate) or polystyrene and poly (tert-butyl methacrylate) obtaining (PS-PMMA) and (PS-PtBMA) block copolymers [11]. Inorganic Janus particle combine metal, metal oxide or silica obtaining for example Au-TiO_2 [12], Au-SiO_2 [13], Au-Fe_3O_4 [14], CuO-CuS [15]. Hybrid (polymeric-inorganic) Janus particles have also been synthesized such as PS-Ag [16], PS-Fe [4], Resin-SiO_2 [17]. Each Janus particle category presents some advantages depending on the field of applications. All of them can be obtained with different architectures including spherical, cylindrical, disk-like, dumbbell-like and ribbon shapes [10]. Janus particles can be fabricated using different techniques as polymer self-assembly [18] and photo-polymerization [19] for polymeric materials whereas inorganic ones are prepared by spin-coating [20] or physical vapor deposition (PVD) [21].

Physical vapor deposition technique is particularly effective to master the thin films morphology and composition by controlling the atmosphere composition at low pressure and

the particle flux directivity [22-23]. Moreover, combining GLancing Angle Deposition (GLAD) [24] with PVD allows creating innovative structures characterized by a high porosity and a columnar aspect. Spherical Janus particles have been obtained with PVD technique combined or not with GLAD. For example, platinum hemispheres have been deposited on silica colloids [21] and polystyrene particle have been coated with gold firstly and carbon afterwards, forming a cap on the upside of the particle [25]. However, the growth of columnar nanostructured thin films associating PVD and GLAD with two different materials and leading to a Janus-like structure has been poorly explored and still remains a challenging task. Different parameters have to be adjusted including not only the elaboration conditions (pressure, temperature, oblique angle of deposition) [26] but also the choice of deposited materials (self-diffusion energy, atomic number, etc.). Different researches have been performed on thin films prepared by GLAD with two different elements like W-Cu [27], Ti-Ag [28] and Si-Ag [29] leading to Janus structures for some given operating conditions.

In this paper, we focus on W-Mo thin films co-deposited by magnetron sputtering using two different targets: tungsten and molybdenum to succeed in obtaining a Janus structure. Janus-like structure obtained in thin films by PVD can be considered as an extreme example of segregation with both metallic half columns separated by frank interfaces. Previous investigations have been performed on co-deposited GLAD thin films based on tungsten including W-Ag (the Janus structure was not obtained) [30] and W-Cu (a Janus structure was obtained by means of specific sputtering conditions) [27]. The choice of molybdenum as a second source is based on its self-diffusion energy that is similar to tungsten one [31]. It induces nearly similar atom mobility for both elements, helping to produce Janus structures. In this work, W-Mo thin films are deposited by a GLAD co-sputtering approach. To understand how a Janus-like structure can be obtained, the structural morphology of W-Mo films and the columns growth evolution are studied. The correlation between the columnar architecture and the electrical transport properties is also discussed. It was previously shown that structural and

electrical properties of thin films strongly depend on deposition conditions such as sputtering pressure, angle of sputtering deposition, deposition temperature [26]. The current intensity applied on each target is also a key parameter that modifies the particle flux, changes the elemental composition of the film and therefore influences the electrical and structural properties. In this work, some deposition parameters like sputtering pressure, oblique angle deposition and W target current are maintained for all films. These conditions are the same for the two film series (300 nm and 1 µm thickness). The only variable parameter is the Mo target current intensity, which is varied from 10 to 200 mA. The effect of this Mo target current on W and Mo concentrations is studied and discussed to understand its influence on the morphology, crystallography and electrical properties of tungsten-molybdenum thin films.

2. Material and methods

DC magnetron sputtering is used to deposit W-Mo thin films on glass and silicon substrates from two metallic targets: tungsten and molybdenum (Fig. 1), both having 99.9 % of purity and 51 mm diameter. They are located inside a 40 L homemade vacuum chamber with a base pressure below 10^{-5} Pa. The distance between the substrates and the centers of W and Mo targets are 65 mm and 95 mm, respectively. These targets are co-sputtered at room temperature in a pure argon atmosphere with a flow rate of 4.4 sccm and a sputtering pressure of 0.33 Pa. Deposition angles used in this study for the tungsten (α_W) and molybdenum (α_{Mo}) are both equal and fixed at $\alpha_W = \alpha_{Mo} = 80°$. All substrates (silicon and glass) are grounded during depositions, with no external heating. They are cleaned with acetone and ethanol before thin films deposition (no etching procedure before running deposition). W-Mo thin films are prepared using a fixed W target current I_W = 140 mA (W target power = 1.8 W.cm^{-2}) and various Mo target currents I_{Mo} between 10 mA (Mo target power = 0.125 W cm^{-2}) and 200 mA (Mo target power = 2.82 W cm^{-2}). For each Mo target current, the films thickness is checked with a Tencor Alpha Step IQ profilometer. The deposition time is adjusted to obtain similar thickness for each sample

series (thickness of 300 nm and 1 µm).

Structural analysis is realized on the films deposited on silicon substrates. The morphology is studied using a scanning electron microscope (SEM) JEOL JSM 7600F to observe the surface and cross-section of the films. Energy dispersive X-ray spectrometry (EDX) is performed during SEM surface observations to determine the atomic concentration of W and Mo for all samples and at different positions along the film. The crystallographic structure is determined by X-ray diffraction (XRD) technique. Measurements are carried out using a Bruker D8 focus diffractometer with a copper X-ray tube (Cu $\lambda_{K\alpha1,2}$ = 0.15425 nm) with a Bragg-Brentano configuration. Scans are performed with 2θ angle from 20° to 120° with a step of 0.0204° per 1 s. The microstructural analysis is also performed using a JEOL 2100 FEG transmission electron microscope (TEM) operating at 200 keV. Before TEM observations, a sample preparation is carried out using the standard sandwich technique. TEM specimen is polished, dimpled down until a thickness around 10 µm and argon ion milled to electron transparency. TEM images are analyzed using GATAN Digital Micrograph software and their simulations are obtained with the Java Electron Microscopy Software (JEMS) [32]. The elemental chemical composition is also determined in scanning (STEM) mode using an EDX detector BRUKER Quantax XFlash 5030T SDD. The electrical resistivity measurements are carried out at room temperature using the four-probe van der Pauw method. The electrical anisotropy defined as the ratio between electrical resistivity measured following perpendicular and parallel directions of particle fluxes [33] is also determined.

3. Results and discussion

3.1 Microstructural analysis

Cross-section and surface observations performed at the center of the samples are shown in Fig. 2 and 3, respectively. No differences of morphology are pointed out between the center and the other positions of the samples except at the extremities. Despite the variation of Mo

target current I_{Mo}, all thin films present a porous and columnar aspect, with columns inclined towards W target (Fig. 2). Cross-section observations clearly point out a columnar structure with separated and inclined columns towards W target where the inclination is characterized by the columnar tilt angle β (angle between the normal to the substrate surface and the columns direction). The columns also present an increasing width with the films thickness [34]. This is related to the extinction of some columns due to the shadowing effect characteristic of the GLAD technique [26, 35]. Vanishing of some columns in favor of the biggest can be noticed whatever the Mo target current, especially when the films thickness changes from 300 nm to 1 µm (Fig. 2). The column extinction process (due to shadowing effect) typically encountered with the single GLAD sputtering also evidences in GLAD co-sputtering. Keeping the same sputtering conditions and varying Mo target current lead to straighten the columns orientation whatever the films thickness (Table 1). At low Mo target current, the column angle β presents higher inclination around 35° and 30° for 300 nm and 1 µm, respectively. β decreases as I_{Mo} rises on the same way for both thicknesses until reaching 3° for 300 nm and 9° for 1 µm. This columnar aspect is also reported for molybdenum thin films deposited at 80° with similar sputtering conditions (pressure, α angle) [36]. Columns of GLAD films prepared with a single W target are as expected oriented towards this target [37], but the introduction of a second target (e.g., molybdenum) can change this column tilting as a function of the sputtering conditions.

Besides a similar columnar growth, W and Mo atoms are also characterized by a quasi-similar surface mobility characterized by a self-diffusion length Λ [38] thermally activated following Eq. (1):

$$\Lambda = \frac{1}{2}\sqrt{\frac{a_h^2\, a_d\, \omega}{r}}\sqrt{exp\left(\frac{-E_d}{k_B\, T}\right)} \quad (1)$$

where a_h is the average distance between atoms, i.e. close to the lattice spacing (m), a_d the distance of adatom moving from one adsorption site to another one (m), ω the lattice vibration

frequency (s^{-1}), r the deposition rate (m s^{-1}), k_B the Boltzmann constant (1.38×10^{-23} J K^{-1}), T the surface temperature (K) and E_d the surface diffusion activation energy (J). For W and Mo, Ed is nearly the same with 1.22 and 1.20 eV, respectively [31], which corresponds to a similar self-diffusion length. Therefore, as both W and Mo thin films are columnar when deposited separately and as their self-diffusion length is almost similar, a simultaneous deposition of W and Mo leads to a real columnar growth competition between W and Mo. With a fixed W target current (I_W = 140 mA), the Mo target current appears to be the key parameter that allows W or Mo flux to dominate and impose the columns orientation towards its target direction. However, the particle flux domination is also related to the geometry of the vacuum chamber. The distance between the targets (W and Mo) and the substrate is different (65 mm and 95 mm, respectively), despite they present practically the same sputtering yield (0.517 and 0.533 for W and Mo, respectively for an Ar^+ energy of 500 eV [39]). Therefore, quasi-vertical columns are obtained for a Mo target current intensity equal to 200 mA, despite a current intensity of only 140 mA applied to W target.

Top-view observations (Fig. 3) confirm the columnar, porous and rough morphology of W-Mo thin films. As previously observed with cross-section SEM, they also confirm that the width of the columns strongly increases with the thickness. The morphology also evolves for both thicknesses as I_{Mo} rises. At lower I_{Mo}, the main columns exhibit little nanocolumns deposited on them. As I_{Mo} increases, the width of these secondary nanocolumns increases. It is also worth noticing that smaller columns are produced for 300 nm thick films deposited with I_{Mo} = 200 mA. For these operating conditions, Mo and W fluxes compete against each other. The W growth prevailing for the lowest Mo target currents gives rise to the fanning and broadening effects of the column sections perpendicularly to the W and Mo fluxes. As I_{Mo} increases, Mo atoms impinging on the growing columns disturb the W growth leading to a less one way feed of particles and thus, bundling phenomenon of the columns is hindered.

At higher Mo target currents (I_{Mo} = 200 mA, thickness = 1 µm), some clear ridges are

pointed out at the columns summit which can presume a separation between W and Mo inside the columns. Moreover, the columns are less inclined and appear to be practically vertical. These films present also an asymmetric morphology for both thicknesses and whatever the Mo target current. The columns show elliptical sections that are connected along the perpendicular direction to W and Mo particle fluxes. This elliptical shape is enhanced for thicker films corresponding to a more anisotropic structure for higher thickness. W and Mo columnar thin films singly deposited with similar conditions have been reported to present the same anisotropic form [37, 40]. Thin films porosity and columns anisotropy are characteristic of GLAD deposition especially when performed at grazing angles ($\alpha = 80°$) [41]. This is strongly linked to the self-shadowing effect magnified at higher oblique angle deposition. The asymmetric microstructure of the columns is more specifically related to the bundling phenomenon that was mentioned in previous studies [42-43]. This phenomenon is based on the lateral connection of the columns in a direction perpendicular to the particle fluxes. This lateral growth is linked to a preferential trapping mechanism [44] that makes the lateral growth more efficient until the columns coalesce. The shadowing effect, intrinsic to the GLAD process, is also one of the important properties that lead to an asymmetric structure as it prevents the particle deposition in some positions along the parallel flux direction.

Composition of W-Mo thin films and atomic concentration ratio are determined using SEM-EDX (Table 2). All measurements are performed for both thicknesses at the center of the films. The W and Mo atomic concentrations appear to be strongly influenced by the Mo target current as shown in Fig. 4. This is particularly significant for the lowest I_{Mo} values, i.e., below 50 mA. With a fixed I_W and an increasing I_{Mo}, the atomic concentration ratio [W]/[Mo] decreases for both thicknesses (300 nm and 1 μm) with a same behavior. The comparison of the ratio values points out a strong difference for both thicknesses at lower current. At lowest Mo target current (I_{Mo} = 10 mA), the highest ratio is obtained with values close to 24 and 49 for 300 nm and 1 μm, respectively. As I_{Mo} increases from 20 to 50 mA, the gap ratio is gradually

reduced until obtaining similar atomic concentrations at I_{Mo} = 200 mA. The variation of the atomic concentration ratio can be indirectly connected to the evolution of the column angle β with I_{Mo} increase. For the lowest Mo target currents, the columns present higher inclination with a β column angle around 36° and 33° for 300 nm and 1 µm, respectively, close to the value obtained for pure W thin films (β = 39° whatever the films thickness) [37]. As a result, a low Mo target current does not disturb the growth of W columns leading to comparable values of β column angle when the deposition is performed with one W target or two W and Mo targets. W-Mo thin films deposited at the lowest I_{Mo} values are mainly composed of W. Indeed, a ratio of 49 corresponds to the presence of only 2 at. % of Mo. Therefore, the W atoms flux clearly prevails for I_{Mo} = 10 mA. In contrast, the atomic concentration ratio becomes nearly equivalent for both thicknesses at highest Mo target current (I_{Mo} = 200 mA) with a value close to 1, which means an equivalent W and Mo atomic concentration.

3.2 Crystallographic analysis

XRD analyses are carried out on W-Mo thin films to obtain information about the crystallographic structure evolution as function of Mo target current (Fig. 5). XRD results show different diffracted intensities for the films deposited with 300 nm and 1 µm thickness. The diffracted signals for both thicknesses mainly appear at two positions close to 2θ = 35° and 40°. An evolution of the relative intensity of these peaks is pointed out, the first ones being more intense than the second ones for the films deposited at 300 nm. The occurrence of these peaks is attributed to the presence of the two different α and β phases of W. Despite the higher Mo target current applied for the different thicknesses, peaks corresponding to α-W and Mo (110) cannot be distinguished. A slight asymmetry of the peaks towards the higher angles is only pointed out. This is explained by the same crystallographic structure (body-centered cubic) and very close lattice parameters between Mo and α-W (a_W = 0.31652 nm and a_{Mo} = 0.31470 nm). It implies quasi-identical 2θ angles of diffracted signals for both elements (theoretical positions

of α-W (110) and Mo (110) are 2θ = 40.26° and 40.51°, respectively). Moreover, recorded peaks are not clearly defined with a quite broad shape, leading to a more difficult discrimination between W and Mo.

For XRD patterns of 300 nm thick films (Fig. 5 (a)), the first detected peak around 2θ = 35.5° corresponds to the (200) planes of the body-centered cubic (bcc) β-W phase (2θ = 35.5°, ICDD-pdf # 00-047-1319). The second detected one is asymmetric and larger than the first one at 2θ = 39.5° - 40.5°. This asymmetric behavior is linked to the detection of the (210) planes of the β-W phase (2θ = 35.525°) and of the (110) planes of the α-W phase (2θ = 40.265°, ICDD-pdf # 00-004-0806), respectively. As the Mo target current increases, the β-W (200) peak becomes more intense while the β-W (210) peak reduces and vanishes with a further increase of Mo target current. Similarly, no modifications on the α-W (110) and/or Mo (110) peak intensity are reported. These results show that β-W phase predominates at 300 nm with a preferential orientation along the (200) planes. On the other hand, the films prepared with higher thickness (1 μm) present two peaks, at similar positions but with opposite relative intensities (Fig. 5(b)). The first one pointed out around 2θ = 35.5° is also attributed to the (200) planes of β-W phase and the second one close to 2θ = 40° corresponds to the (110) planes of the α-W phase and/or (110) of the Mo phase. The different W phases (α and β) are detected whatever the applied Mo target current. A slight increase of β-W (200) peak intensity versus I_{Mo} is noticed whereas α-W and/or Mo (110) peak intensity strongly increases at the same time. For 1 μm thickness, the predominance of α-W and/or Mo is noticed with a preferential orientation along the (110) planes. Furthermore, a small shift of the (110) peak position to the higher diffracted angles is observed from 2θ = 40.27° for I_{Mo} = 10 mA to 2θ = 40.32° for I_{Mo} = 200 mA. As the theoretical Mo (110) peak position is 2θ = 40.51°, it can indicate a small influence of the Mo target current on the peak position with a shift from α-W (110) to Mo (110), suggesting the co-existence of α-W and Mo phases. A shift to lower 2θ angles from equilibrium position has been reported for Mo thin films deposited at low sputtering pressure (0.88 Pa) [45]. In our W-Mo

films 1 µm thick, the position of the (110) Mo peak agrees with this shift since it is observed at 2θ close to 40.3°.

Formation of α-W and β-W (metastable A-15 structure) phases depends on the deposition conditions as films thickness, deposition rate, substrate temperature and/or sputtering pressure of inert gas [46-49]. The β-W phase is a metastable phase with the A-15 structure formed by O atoms situated at the body center lattice sites and W atoms occupying two lattice sites of each unit cell face. In contrast, the α-W phase is considered as a thermodynamically stable phase with all lattice sites occupied by a W atom. The difference between the two W phases structure generates different lattice parameters equal to a = 0.31652 nm for α-W and a = 0.5040 nm for β-W. The β-W phase is distinguished by the presence of O atoms. Their concentration should never surpass 25 at. % that correspond to W_3O stoichiometry but is regularly reported below 10 at. % [50]. It is well admitted that the β-W phase is stabilized by the incorporation of oxygen as impurities [46-50]. The occurrence of the metastable β-W phase and its transformation to stable α-W phase is dependent on many deposition parameters [51] but also on the deposition technique itself. Indeed, the presence of β-W phase is strongly influenced by the normal or oblique incidence of the flux as well as by the eventual application of a rotation to the substrate. With normal incidence, β-W evolves to α-W as the thickness of the deposit increases, even if no critical thickness value is reported [49, 52]. Using GLAD conditions (high oblique incidence angle combined with substrate rotation), Karabacak et al. reported the creation of nanorods with only the β-W phase [53]. The predominance of β-W or α-W phases has been related to a more or less influence of the self-shadowing effect as well as to different adatom mobilities. However, it is possible to overcome the effect of self-shadowing and to obtain α-W nanorods in GLAD conditions with flipping rotation deposition mode [54]. In our study, thin films are deposited using oblique incidence conditions with a high angle ($\alpha_W = \alpha_{Mo} = 80°$) but without any rotation of the substrate. XRD results indicate that the β-W phase is predominant for samples grown at 300 nm and evolves to the α-W one for samples grown at

1 µm. In the first case, the occurrence of the β-W phase is favored by the self-shadowing effect, characteristic of oblique incidence deposition. However, at higher thickness, an evolution to the stable α-W phase is pointed out as previously reported for thick samples deposited with normal incidence [53]. A similar behavior is obtained for GLAD W thin films grown with similar conditions, the occurrence of α-W phase being reported for W films thicker than 450 nm [37].

3.3 Nanostructural analysis

High resolution transmission electron microscopy (HRTEM) and scanning transmission electron microscopy combined with energy dispersive X-ray spectrometry (STEM-EDX) experiments are also carried out on the 300 nm thick W-Mo thin film deposited with I_{Mo} = 200 mA. This sample has been chosen since equivalent W and Mo atomic concentrations have been pointed out by SEM-EDX. Therefore, it can facilitate HRTEM and STEM-EDX analyses to detect the presence of W and Mo and study their distribution in the columns. Figure 6(a) confirms the columnar aspect previously reported by SEM observations. The columns present crystallized areas as shown by HRTEM images (Fig. 6(b) and (c)). The combination of fast-Fourier transform patterns realized on the HRTEM images with simulated patterns of W (α and β phases) and Mo allows to point out the presence of different zone axes and phases. In Fig. 6(b), the [001] zone axis corresponds to β-W phase with crystallographic planes {200} while in Fig. 6(c), the [001] zone axis can be related to α-W and/or Mo phase with perpendicular crystallographic planes {110} (α-W and Mo both adopt the bcc structure with very close lattice constant with a_W = 0.31652 nm and a_{Mo} = 0.31470 nm, respectively). These results confirm the occurrence of α-W (and/or Mo) and β-W phases as previously characterized by XRD. Moreover, EDX points performed on crystallized areas allows discriminating between α-W and Mo, which are both pointed out separately. W and Mo distribution is determined by STEM-EDX in order to bring to the fore a Janus structure. The darker and brighter areas inside a given column visible in dark-field STEM image can be associated to an eventual Janus structure (Fig.

6(d)). The corresponding hypermapping image (Fig. 6(e)) which superposes W and Mo maps shows a clear separation of W and Mo elements with a net interface between them inside the column. This distribution is observed in their whole length from the silicon substrate. The presence of Janus structure has been reported for all columns observed in sufficiently thinned areas (without any superposition of several columns). These results confirm the creation of a Janus structure with W-Mo films using our deposition conditions.

Such a Janus structure has ever been obtained before for other systems as W-Cu [27] and Ta-Si [55] prepared by GLAD co-sputtering. W-Cu thin films present a Janus-like structure but only with a net dominance of W (75 at. %) inside the columns. This is not the case for W-Mo thin films characterized by a Janus structure but also equivalent W and Mo concentrations. Similar results were reported for Ta-Si thin films deposited on silica spheres and exhibiting a Janus structure with different architectures. These systems are prepared practically with the same sputtering conditions (pressure below 0.5 Pa, two facing targets). Therefore, sputtering parameters are key factors to obtain a Janus structure. More particularly, the working pressure appears to be the main parameter to consider. The chosen value equal to 0.33 Pa induces a ballistic regime with highly energetic and directional particles [56]. On the other hand, the choice of the materials to create a Janus structure must also be considered, especially the columnar aspect of each material deposited alone with the same conditions (pressure, oblique angle). GLAD W and Mo films grow following the same columnar aspect [37, 57]. This is not the case for Ag [58] for which the columns are not so clearly formed and bundled. For W-Ag films [30], columns are mainly produced by W and Ag is deposited as grains around the columns. Immiscibility is also a relevant parameter [59], which has to be taken into account to choose the materials for the creation of a Janus structure. The study of the two different systems W-Mo and W-Ag shows that immiscibility is not completely required to select the deposited elements. W and Ag are immiscible but their co-deposition does not give rise to a Janus structure. On the other hand, W and Mo are miscible and their co-deposition can create a Janus

structure, especially favored by balanced and symmetric W and Mo particle fluxes. This structure is also reachable for other systems as previously reported for W-Cu couple tuning again each target current and implementing ballistic sputtering conditions, i.e. a low sputtering pressure [27]. However, the preparation of clear bi-component patterns may become a challenging task when metals exhibiting a low surface self-diffusion energy are involved (e.g., Ag in Ti-Ag films [28]).

3.4 Electrical properties and anisotropy

Using the van der Pauw method, DC electrical resistivity is measured at room temperature for all W-Mo thin films deposited on glass substrate. These measurements are carried out to study the electrical properties of W-Mo films and to better understand the effect of Mo target current and thickness variations. Figures 7(a) and (b) show the DC electrical resistivity and electrical anisotropy at room temperature vs. Mo target current for both thicknesses. The lowest DC electrical resistivities obtained for I_{Mo} = 10 mA are $\rho = 4.6\times10^{-6}$ and 7.1×10^{-7} Ω m for 300 nm and 1 µm, respectively. These values are 1 to 2 orders of magnitude higher than that of bulk W and Mo ($\rho_W = 5.39\times10^{-8}$ Ω m and $\rho_{Mo} = 5.47\times10^{-8}$ Ω m at room temperature) [60]. This is linked to the higher porosity typically produced for GLAD thin films using high oblique incidence angles. The electron scattering phenomenon becomes more important due to the increased presence of voids [61].

DC electrical resistivity vs. Mo target current presents a linear evolution for both thicknesses (300 nm and 1 µm) as shown in Fig. 7(a). For the films with 300 nm thickness, an increase of electrical resistivity is noticed with I_{Mo} from $\rho = 4.6\times10^{-6}$ Ω m for I_{Mo} = 10 mA to $\rho = 1.6\times10^{-5}$ Ω m for I_{Mo} = 200 mA and the linear evolution gives rise to a slope around 6.47×10^{-8} Ω m mA^{-1}. The same trend is obtained for the 1 µm films with $\rho = 7.1\times10^{-7}$ Ω m for I_{Mo} = 10 mA and $\rho = 1\times10^{-5}$ Ω m for I_{Mo} = 200 mA with practically the same slope around 4.55×10^{-8} Ω m mA^{-1}. As Mo is more resistive compared to W, this linear evolution can be explained by the

gradual increase of Mo amount in the films whatever the film thickness. Both thickness series present a similar linear evolution as shown by the little slope difference being related to the quasi-similar atomic concentration between W and Mo. Despite the same electrical resistivity evolution for both thicknesses, the 300 nm films are systematically more resistive than the 1 µm films. Previous works have shown that the electrical resistivity depends on the crystallographic structures of the elements present in the film [47, 51, 53]. In our study, W-Mo thin films exhibit different tungsten crystallographic phases (β-W mainly for 300 nm and α-W for 1 µm). As β-W phase resistivity is one order of magnitude higher than that of α-W [47, 51, 53], 300 nm films are more resistive compared to the 1 µm ones. Thin films thickness is also an important factor having an impact on electrical resistivity measurements. Therefore, different studies [37, 62] have shown that electrical resistivity decreases with thin films thickness. All these factors explain the higher electrical resistivity measured for all 300 nm films compared to the 1 µm ones.

The electrical anisotropy A corresponds to the ratio between electrical resistivity measured in the direction parallel ($\rho_{//}$) and perpendicular ($\rho_{\perp}$) to the particle flux [33]. The electrical anisotropy ratio presents the same evolution for both thicknesses as shown in Fig. 7(b). The ratio increases with Mo target current from A = 1.3 (I_{Mo} = 10 mA) to A = 1.7 (I_{Mo} = 200 mA) for 300 nm films and from A = 1.4 (I_{Mo} = 10 mA) to A = 1.8 (I_{Mo} = 200 mA) for 1 µm films. This electrical anisotropy is higher for the 1 µm films, which can be related to the morphological anisotropy of the thin films as shown from SEM observations (Fig. 3). Due to the widening of the columns as the thickness increases and assuming the lateral growth of the films, the cross-section of the columns becomes more elliptic with the thickness. Furthermore, the Mo target current also influences the surface anisotropy as the columns present more anisotropic forms (elongated shape which is emphasized). This is related to the increase of deposited particle that leads to a more important lateral growth of the columns due to the shadowing effect. This anisotropic growth correlates with electrical anisotropy and surface

anisotropy. All these results show some correlations between thin films structure (morphology and crystallography) and electrical response (resistivity and anisotropy).

4. Conclusion

W-Mo thin films are prepared by simultaneous GLAD co-sputtering with two W and Mo targets, tilted with an angle $\alpha = 80°$. With a fixed W target current (I_W = 140 mA) and various Mo target currents (I_{Mo} between 10 and 200 mA), two different thicknesses are prepared: 300 nm and 1 µm. The two samples series present porous and columnar aspects due to the self-shadowing effect, characteristic of GLAD. The columns are more or less inclined, becoming perpendicular to the substrate surface for the highest Mo target currents. This architecture variation is linked to the increased Mo flux, offsetting the W one. An anisotropic form of the columns is observed whatever the thickness of the films with an elongated shape of the columnar cross-sections and sharpened apexes in the direction perpendicular to W and Mo fluxes, particularly for higher Mo target currents and thicker films. XRD analyses point out a thickness effect on the crystallographic structure of the films as β-W phase predominates for 300 nm while it evolves to α-W phase for 1 µm. Since α-W and Mo phases both adopt the bcc crystallographic structure with very close lattice parameters, no clear diffracted signals allow clearly distinguishing each metal by XRD. However, TEM analyses support the presence of different α-W, α-Mo and β-W crystallized areas in a same column whereas STEM-EDX analyses confirm the occurrence of a well-separated W and Mo distribution inside a given column following its length. So, W-Mo thin films are characterized by a Janus-like structure under those growing conditions, confirming that immiscibility character of the deposited elements is not the key parameter to obtain a Janus-like structure. The electrical resistivity linearly increases as a function of the Mo target current and presents the same behavior for both thicknesses. The electrical anisotropy shows some correlations with anisotropic morphology of the columns with a more elliptical cross-section of the columns as the films thickness or Mo

target current rises.

Last but not least, these Janus-like structures produced in W-Mo thin films by GLAD co-sputtering bring together two different materials in a segregated manner at the nanoscale, thus combining different metallic properties in single entity. Such architectures are typically required for applications implementing anisotropic behaviors of surfaces and interfaces such as gas sensing, bio-sensing, catalysis or microfluidics where the association of two-well separated compounds may provide enhanced performances of devices working in liquid or gaseous media.

Acknowledgements

This work has been supported by the Region Bourgogne Franche-Comté and by EIPHI Graduate School (Contract ‘ANR-17-EURE-0002’).

References

[1] C. Casagrande, P. Fabre, E. Raphael, M. Veyssie, Janus Beads: Realization and Behaviour at Water/Oil Interfaces, Europhys. Lett. 9 (1989) 251–255. https://doi.org/10.1209/0295-5075/9/3/011

[2] P.G. de Gennes, Soft Matter, Rev. Mod. Phys. 64 (1992) 645–648. https://doi.org/10.1103/RevModPhys.64.645.

[3] K.P. Yuet, D.K. Hwang, R. Haghgooie, P.S. Doyle, Multifunctional Superparamagnetic Janus Particle, Langmuir 26 (2010) 4281–4287. https://doi.org/10.1021/la903348s

[4] S.K. Smoukov, S. Gangwal, M. Marquez, O.D. Velev, Reconfigurable responsive structures assembled from magnetic Janus particle, Soft Matter 5 (2009) 1285–1292. https://doi.org/10.1039/B814304h

[5] A. Kirillova, C. Schliebe, G. Stoychev, A. Jakob, H. Lang, A. Synytska, Hybrid Hairy Janus Particle Decorated with Metallic Nanoparticle for Catalytic Applications, ACS Appl. Mater. Interfaces 7 (2015) 21218–21225. https://doi.org/10.1021/acsami.5b05224

[6] M.D. McConnell, M.J. Kraeutler, S. Yang, R.J. Composto, Patchy and Multiregion Janus Particle with Tunable Optical Properties, Nano Lett. 10 (2010) 603–609. https://doi.org/10.1021/nl903636r

[7] Y. Duan, X. Zhao, M. Sun, H. Hao, Research Advances in the Synthesis, Application, Assembly, and Calculation of Janus Materials, Ind. Eng. Chem. Res. 60 (2021) 1071−1095. https://doi.org/10.1021/acs.iecr.0c04304

[8] M. Yoshida, K.-H. Roh, S. Mandal, S. Bhaskar, D. Lim, H. Nandivada, X. Deng, J. Lahann, Structurally Controlled Bio-hybrid Materials Based on Unidirectional Association of Anisotropic Microparticle with Human Endothelial Cells, Adv. Mater. 21 (2009) 4920–4925. https://doi.org/10.1002/adma.200901971

[9] Y. Ye, J. Luan, M. Wang, Y. Chen, D.A. Wilson, F. Peng, Y. Tu, Fabrication of Self-Propelled Micro- and Nanomotors Based on Janus Structures, Chem. Eur. J. 25 (2019) 1–19. http://dx.doi.org/10.1002/chem.201983762

[10] X. Pang, C. Wan, M. Wang, Z. Lin, Strictly Biphasic Soft and Hard Janus Structures: Synthesis, Properties, and Applications, Angew. Chem. Int. Ed. 53 (2014) 5524–5538. https://doi.org/10.1002/anie.201309352

[11] A. Walther, A.H.E. Muller, Janus particle, Soft Matter 4 (2008) 663–668.

https://doi.org/10.1039/B718131K

[12] S. Pradhan, D. Ghosh, S. Chen, Janus Nanostructures Based on Au−TiO_2 Heterodimers and Their Photocatalytic Activity in the Oxidation of Methanol, ACS Appl. Mater. Interfaces 1 (2009) 2060–2065. https://doi.org/10.1021/am900425v

[13] L. Su, L. Wang, J. Xu, Z. Wang, X. Yao, J. Sun, J. Wang, D. Zhang, Competitive Lateral Flow Immunoassay Relying on Au–SiO_2 Janus Nanoparticle with an Asymmetric Structure and Function for Furazolidone Residue Monitoring, J. Agric. Food Chem. 69 (2021) 511−519. https://doi.org/10.1021/acs.jafc.0c06016

[14] L. Landgraf, P. Ernst, I. Schick, O. Köhler, H. Oehring, W. Tremel, I. Hilger, Anti-oxidative effects and harmlessness of asymmetric Au@Fe_3O_4 Janus particle on human blood cells, Biomaterials 35 (2014) 6986−6997. https://doi.org/10.1016/j.biomaterials.2014.04.111

[15] D. Li, Y. He, S. Wang, On the Rotation of the Janus CuO/CuS Colloids Formed at a Pickering Emulsion Interface, J. Phys. Chem. C 113 (2009) 12927−12929. https://doi.org/10.1021/jp903262c

[16] S. Yang, P.J. Hricko, P.-H. Huang, S. Li, Y. Zhao, Y. Xie, F. Guo, L. Wang, T.J. Huang, Superhydrophobic Surface Enhanced Raman Scattering Sensing Using Janus Particle Arrays Realized by Site-Specific Electrochemical Growth, J. Mater. Chem. C 2 (2014) 542–547. https://doi.org/10.1039/C3TC31635A

[17] S.-H. Kim, A. Abbaspourrad, D.A. Weitz, Amphiphilic Crescent-Moon-Shaped Microparticle Formed by Selective Adsorption of Colloids, J. Am. Chem. Soc. 133 (2011) 5516–5524. https://doi.org/10.1021/ja200139w

[18] L. Cheng, G. Zhang, L. Zhu, D. Chen, M. Jiang, Nanoscale Tubular and Sheetlike Superstructures from Hierarchical Self-Assembly of Polymeric Janus Particle, Angew. Chem. 47 (2008) 10171–10174. https://doi.org/10.1002/ange.200803315

[19] S. Yang, F. Guo, B. Kiraly, X. Mao, M. Lu, K.W. Leong, T.J. Huang, Microfluidic synthesis of multifunctional Janus particle for biomedical applications, Lab Chip 12 (2012) 2097–2102. https://doi.org/10.1039/C2LC90046G

[20] A. Kierulf, M. Azizi, H. Eskandarloo, J. Whaley, W. Liu, M. Perez-Herrera, Z. You, A. Abbaspourra, Starch-based Janus particle: Proof-of-concept heterogeneous design via a spin-coating spray approach, Food Hydrocolloids 91 (2019) 301–310. https://doi.org/10.1016/j.foodhyd.2019.01.037

[21] R.J. Archer, A.J. Parnell, A.I. Campbell, J.R. Howse, S.J. Ebbens, A Pickering Emulsion Route to Swimming Active Janus Colloids, Adv. Sci. 5 (2018) 1700528 (9 pp). https://doi.org/10.1002/advs.201700528

[22] V. Potin, A. Cacucci, N. Martin, Correlations between structure, composition and electrical properties of tungsten /tungsten oxide periodic multilayers sputter deposited by gas pulsing, Superlattices and Microstructure 101 (2017) 127–137. http://dx.doi.org/10.1016/j.spmi.2016.10.071

[23] V. Potin, A. Cacucci, N. Martin, Correlation between deposition parameters of periodic titanium metal/oxide nanometric multilayers and their chemical and structural properties investigated by STEM-EELS, Micron 101 (2017) 62–68. http://dx.doi.org/10.1016/j.micron.2017.06.008

[24] K. Robbie, M.J. Brett, Sculptured thin films and glancing angle deposition: Growth mechanics and applications, J. Vac. Sci. Technol. A 15 (1997) 1460–1465. https://doi.org/10.1116/1.580562

[25] A. Rashidi, M.W. Issa, I.T. Martin, A. Avishai, S. Razavi, C.L. Wirth, Local Measurement of Janus Particle Cap Thickness, ACS Appl. Mater. Interfaces 10 (2018) 30925−30929. https://doi.org/10.1021/acsami.8b11011

[26] M.M. Hawkeye, M.J. Brett, Glancing angle deposition: Fabrication, properties, and applications of micro- and nanostructured thin films, J. Vac. Sci. Technol. A 25 (2007) 1317–1335. https://doi.org/10.1116/1.2764082

[27] R. El Beainou, N. Martin, V. Potin, P. Pedrosa, M. Arab Pour Yazdi, A. Billard, Correlation between structure and electrical resistivity of W-Cu thin films prepared by GLAD co-sputtering, Surf. Coat. Technol. 313 (2017) 1–7. http://dx.doi.org/10.1016/j.surfcoat.2017.01.039

[28] P. Pedrosa, A. Ferreira, N. Martin, M. Arab Pour Yazdi, A. Billard, S. Lanceros-Méndez, F. Vaz, Nano-sculptured Janus-like TiAg thin films obliquely deposited by GLAD co-sputtering for temperature sensing, Nanotechnology 29 (2018) 355706 (11 pp). https://doi.org/10.1088/1361-6528/aacba8

[29] Y. He, J. Wu, Y. Zhao, Designing Catalytic Nanomotors by Dynamic Shadowing Growth, Nano Lett. 7 (2007) 1369–1375. https://doi.org/10.1021/nl070461j

[30] H. Boukhalfa, V. Potin, N. Martin, Microstructural analysis and electrical behaviours of co-sputtered W–Ag thin films with a tilted columnar architecture, J. Phys. D: Appl. Phys. 54 (2021) 255304 (9pp). https://doi.org/10.1088/1361-6463/abf312

[31] S.Y. Davydov, Calculation of the activation energy for surface self-diffusion of

transition-metal atoms, Phys. Solid State 41 (1999) 8–10. https://doi.org/10.1134/1.1130717

[32] P. Stadelmann, JEMS–EMS Java Version CIME-EPFL, Lausanne, Switzerland.

[33] O. Bierwagen, R. Pomraenke, S. Eilers, W.T. Masselink, Mobility and carrier density in materials with anisotropic conductivity revealed by van der Pauw measurements, Phys. Rev. B 70 (2004) 165307–165312. https://doi.org/10.1103/PhysRevB.70.165307

[34] T. Karabacak, J.P. Singh, Y.-P. Zhao, G.-C. Wang, T.-M. Lu, Scaling during shadowing growth of isolated nanocolumns, Phys. Rev. B 68 (2003) 125408–125412. https://doi.org/10.1103/PhysRevB.68.125408

[35] D.O. Smith, M.S. Cohen, G.P. Weiss, Oblique-Incidence Anisotropy in Evaporated Permalloy Films, J. Appl. Phys. 31 (1960) 1755–1762. https://doi.org/10.1063/1.1735441

[36] P. Solar, A. Choukourov, J. Hanus, E. Pavlova, D. Slavinska, H. Biederman, Nanocomposite structured thin films by magnetron sputtering at glancing angle deposition, Proceedings of the International Plasma Chemistry Society, Bochum, Germany (2009) 27–31. https://www.ispc-conference.org/ispcproc/papers/286

[37] A. Chargui, R. El Beainou, A. Mosset, S. Euphrasie, V. Potin, P. Vairac, N. Martin, Influence of Thickness and Sputtering Pressure on Electrical Resistivity and Elastic Wave Propagation in Oriented Columnar Tungsten Thin Films, Nanomaterials 10 (2020) 81–99. https://doi.org/10.3390/nano10010081

[38] L. Abelmann, C. Lodder, Oblique evaporation and surface diffusion, Thin Solid Films 305 (1997) 1–21. https://doi.org/10.1016/S0040-6090(97)00095-3

[39] Y. Yamamura, H. Tawara, Energy Dependence of Ion-Induced Sputtering Yields from Monoatomic Solids at Normal Incidence, Research Report NIFS-Data-23 (1995).

[40] R. Krishnan, M. Riley, S. Lee, T.-M. Lu, Vertically aligned biaxially textured molybdenum thin films, J. Appl. Phys. 110 (2011) 064311–064316. https://doi.org/10.1063/1.3638452

[41] M.O. Jensen, M. Brett, Porosity engineering in glancing angle deposition thin films, Appl. Phys. A 80 (2005) 763–768. https://doi.org/10.1007/s00339-004-2878-5

[42] R. El Beainou, A. Garcia-Valenzuela, M. Raschetti, J.M. Cote, R. Alvarez, A. Palmero,

N. Martin, A 4-view imaging to reveal microstructural differences in obliquely sputter-deposited tungsten films, Mater. Lett. 264 (2020) 127381–127384. https://doi.org/10.1016/j.matlet.2020.127381

[43] A. Barranco, A. Borras, A.R. Gonzalez-Elipe, A. Palmero, Perspectives on oblique angle deposition of thin films: From fundamentals to devices, Prog. Mater. Sci. 76 (2016) 59–153. http://dx.doi.org/10.1016/j.pmatsci.2015.06.003

[44] R. Alvarez, C. Lopez-Santos, J. Parra-Barranco, V. Rico, A. Barranco, J. Cotrino, A.R. Gonzalez-Elipe, A. Palmero, Nanocolumnar growth of thin films deposited at oblique angles: Beyond the tangent rule, J. Vac. Sci. Technol. B 32 (2014) 041802–041807. http://dx.doi.org/10.1116/1.4882877

[45] P. Chelvanathan, S.A. Shahahmadi, F. Arith, K. Sobayel, M. Aktharuzzaman, K. Sopian, F.H. Alharbi, N. Tabet, N. Amin, Effects of RF magnetron sputtering deposition process parameters on the properties of molybdenum thin films, Thin Solid Films 638 (2017) 213–219. https://doi.org/10.1016/j.tsf.2017.07.057

[46] J.-S. Lee, J. Cho, C.-Y. You, Growth and characterization of α and β phase tungsten films on various substrates, J. Vac. Sci. Technol. A 34 (2016) 021502–021506. https://doi.org/10.1116/1.4936261

[47] M.J. O'Keefe, J.T. Grant, Phase transformation of sputter deposited tungsten thin films with A15 structure, J. Appl. Phys. 79 (1996) 9134–9141. http://dx.doi.org/10.1063/1.362584

[48] K. Barmak, J. Liu, Impact of deposition rate, underlayers, and substrates on β−tungsten formation in sputter deposited films, J. Vac. Sci. Technol. A 35 (2017) 061516–0615121. https://doi.org/10.1116/1.5003628

[49] I.A. Weerasekera, S. Ismat Shah, D.V. Baxter, K.M. Unruh, Structure and stability of sputter deposited beta-tungsten thin films, Appl. Phys. Lett. 64 (1994) 3231–3233. http://dx.doi.org/10.1063/1.111318

[50] M.J. O'Keefe, J.T. Grant, J.S. Solomon, Magnetron Sputter Deposition of A-15 and Bcc Crystal Structure Tungsten Thin Films, J. Electron. Mater. 24 (1995) 961–967. https://doi.org/10.1007/BF02652968

[51] F.T.N. Vüllers, R. Spolenak, Alpha- vs. beta-W nanocrystalline thin films: A comprehensive study of sputter parameters and resulting materials' properties, Thin Solid Films 577 (2015) 26–34. http://dx.doi.org/10.1016/j.tsf.2015.01.030

[52] S.M. Rossnagel, I.C. Noyan, C. Cabral Jr, Phase transformation of thin sputter-deposited tungsten films at room temperature, J. Vac. Sci. Technol. B 20 (2002) 2047–2051. http://dx.doi.org/10.1116/1.1506905

[53] T. Karabacak, A. Mallikarjunan, J.P. Singh, D. Ye, G.-C. Wang, T.-M. Lu, β-phase tungsten nanorod formation by oblique-angle sputter deposition, Appl. Phys. Lett. 83 (2003) 3096–3098. https://doi.org/10.1063/1.1618944

[54] L. Chen, T.-M. Lu, G.-C. Wang, Creation of biaxial body center cubic tungsten nanorods under dynamic shadowing effect, Thin Solid Films 539 (2013) 65–69. http://dx.doi.org/10.1016/j.tsf.2013.04.151

[55] C.M. Zhou, H.F. Li, D. Gall, Multi-component nanostructure design by atomic shadowing, Thin Solid Films 517 (2008) 1214–1218. http://dx.doi.org/10.1016/j.tsf.2008.05.049

[56] H. Boukhalfa, V. Potin, N. Martin, Ballistic and thermalized regimes to tune structure and conducting properties of W-Mo thin films, Vacuum 204 (2022) 111347–10. https://doi.org/10.1016/j.vacuum.2022.111347

[57] R. Krishnan, M. Riley, S. Lee, T.-M. Lu, Vertically aligned biaxially textured molybdenum thin films, J. Appl. Phys. 110 (2011) 064311–064315. https://doi.org/10.1063/1.3638452

[58] D.A. Gish, F. Nsiah, M.T. McDermott, M.J. Brett, Localized Surface Plasmon Resonance Biosensor Using Silver Nanostructures Fabricated by Glancing Angle Deposition, Anal. Chem. 79 (2007) 4228–4232. https://doi.org/10.1021/ac0622274

[59] ASM Handbook Committee, Metals Handbook, Vol. 8, Metallography, Structures and Phase Diagrams, 8th edition, American Society for Metal, Metals Park, Ohio, (1973).

[60] D.R. Lide, CRC Handbook of Chemistry and Physics, Internet Version 2005, CRC Press, FL, Boca Raton, 2005. https://www.hbcp.chemnetbase.com

[61] A. Besnard, N. Martin, L. Carpentier, B. Gallas, A theoretical model for the electrical properties of chromium thin films sputter deposited at oblique incidence, J. Phys. D 44 (2011) 215301–215308. https://doi.org/10.1088/0022-3727/44/21/215301

[62] E. Elangovan, M.P. Singh, K. Ramamurthi, Studies on structural and electrical properties of spray deposited SnO_2:F thin films as a function of film thickness, Mater. Sci. Eng. B 113 (2004) 143–148. https://doi.org/10.1016/j.mseb.2004.07.072

List of Tables

Table 1:

Columnar tilt angle (β angle) for W-Mo thin films prepared with two thicknesses (300 nm and 1μm) and for different Mo target currents I_{Mo}.

	300 nm	1 μm
Mo target current I_{Mo} (mA)	β angle (± 2°)	β angle (± 2°)
20	35	30
50	29	24
100	20	17
200	3	9

Table 2:

Mo atomic concentrations (at. %) for W-Mo thin films prepared with two thicknesses (300 nm and 1μm) and for different Mo target currents I_{Mo}.

	300 nm	1 μm
Mo target current I_{Mo} (mA)	Mo (± 2%)	Mo (± 2%)
10	4	2
20	7	5
30	11	7
40	15	11
50	17	14
100	34	25
150	43	36
200	52	43

List of figures

images of crystallized areas. (d) and (e) Dark-field STEM and hypermapping images of W-Mo thin film.

Figure 7:

(a) DC electrical resistivity and (b) electrical anisotropy at room temperature for W-Mo thin films prepared with various Mo target currents and for two different thicknesses: 300 nm and 1 μm.

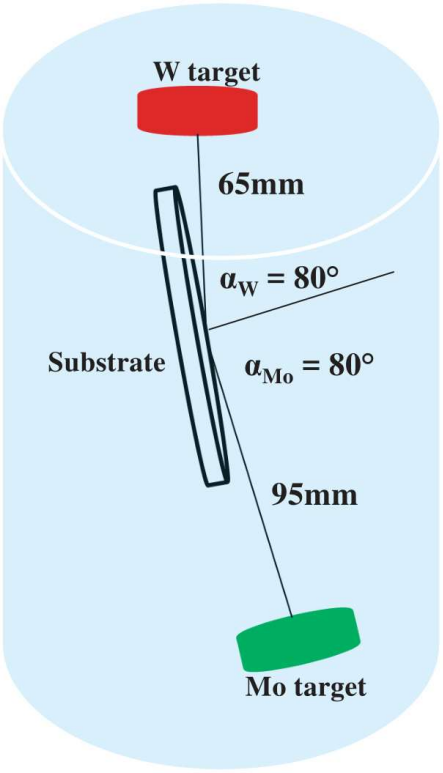

Figure 1

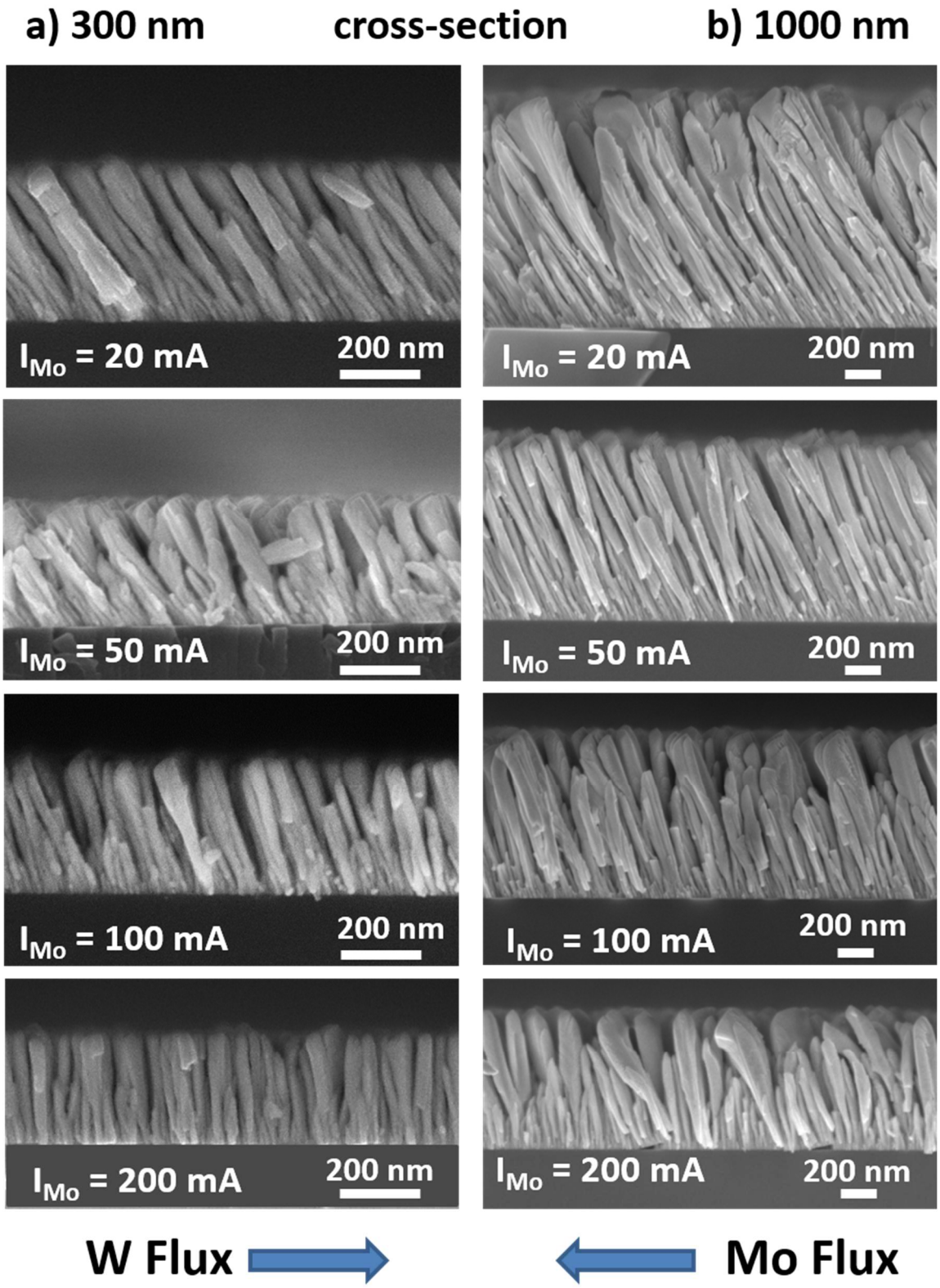
a) 300 nm
cross-section
b) 1000 nm
I_Mo = 20 mA
200 nm
I_Mo = 20 mA
200 nm
I_Mo = 50 mA
200 nm
I_Mo = 50 mA
200 nm
I_Mo = 100 mA
200 nm
I_Mo = 100 mA
200 nm
I_Mo = 200 mA
200 nm
I_Mo = 200 mA
200 nm
W Flux
Mo Flux

Figure 2

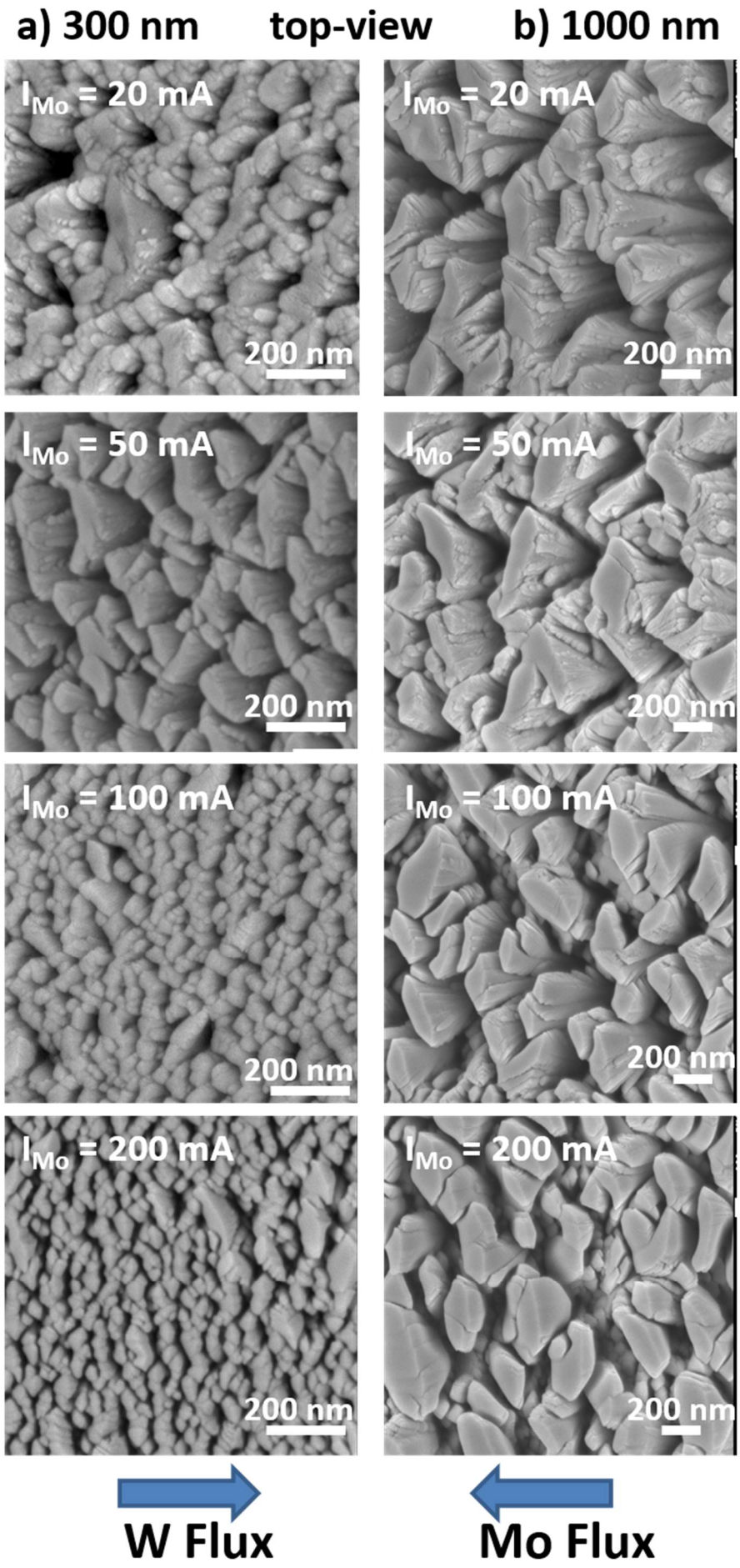
a) 300 nm
top-view
b) 1000 nm
I_{Mo} = 20 mA
200 nm
I_{Mo} = 20 mA
200 nm
I_{Mo} = 50 mA
200 nm
I_{Mo} = 50 mA
200 nm
I_{Mo} = 100 mA
200 nm
I_{Mo} = 100 mA
200 nm
I_{Mo} = 200 mA
200 nm
I_{Mo} = 200 mA
200 nm
W Flux
Mo Flux

Figure 3

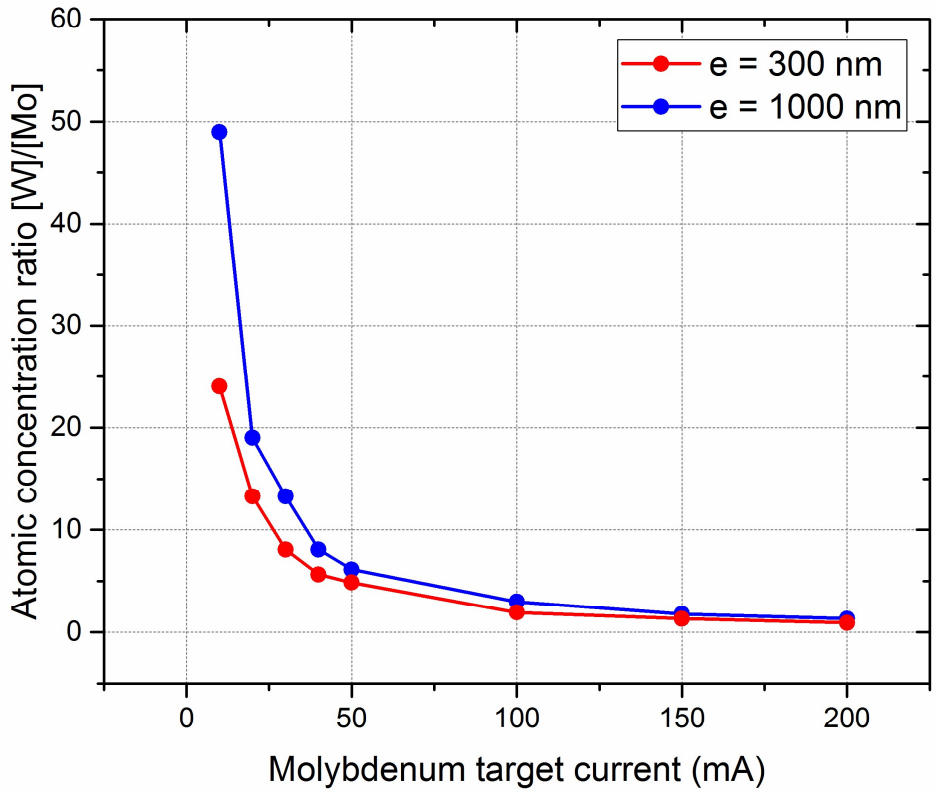
e = 300 nm
e = 1000 nm
Atomic concentration ratio [W]/[Mo]
Molybdenum target current (mA)
0
10
20
30
40
50
60
0
50
100
150
200

Figure 4

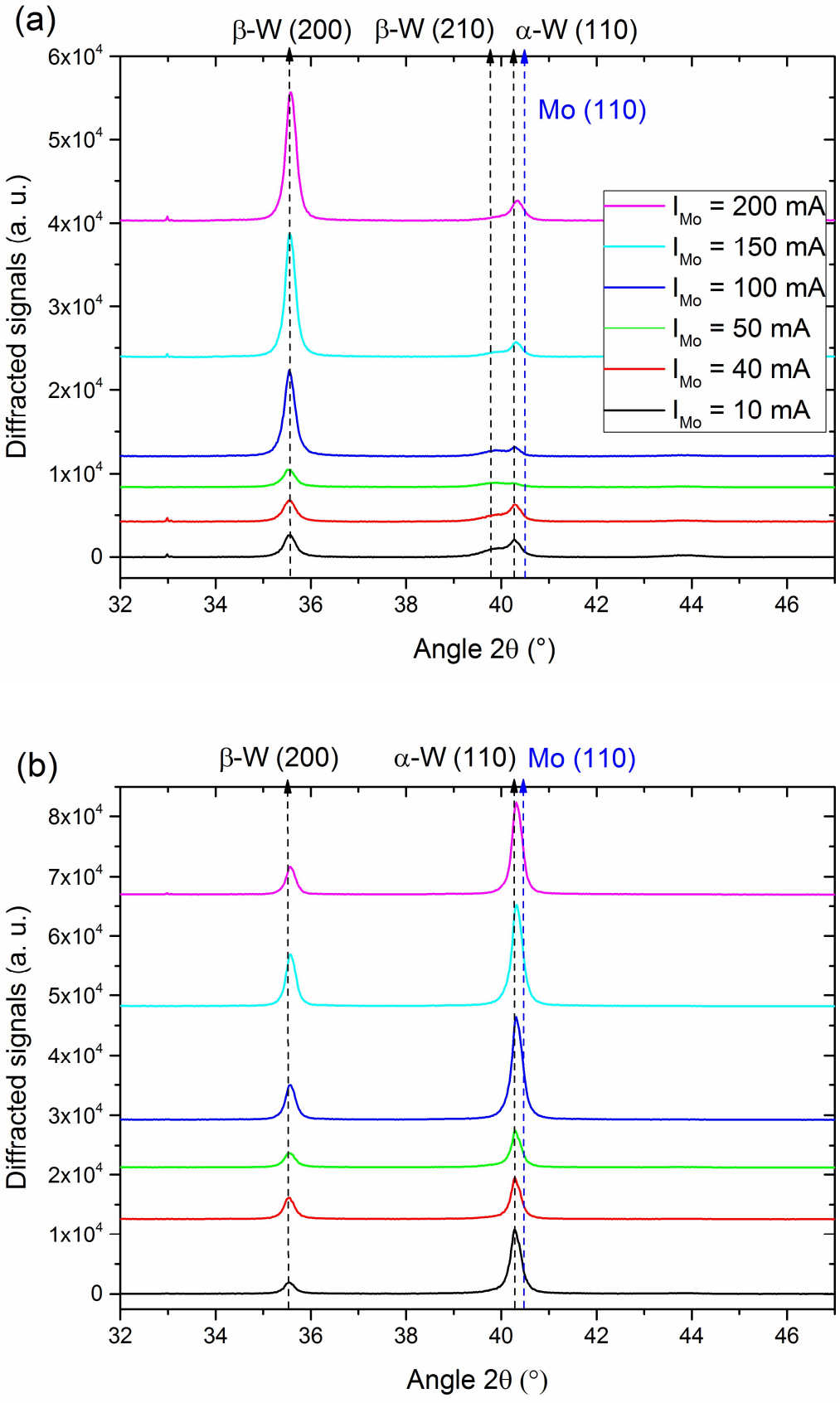
(a)
β-W (200)
β-W (210)
α-W (110)
Mo (110)
Diffracted signals (a. u.)
Angle 2θ (°)
I_Mo = 200 mA
I_Mo = 150 mA
I_Mo = 100 mA
I_Mo = 50 mA
I_Mo = 40 mA
I_Mo = 10 mA
(b)
β-W (200)
α-W (110)
Mo (110)
Diffracted signals (a. u.)
Angle 2θ (°)

Figure 5

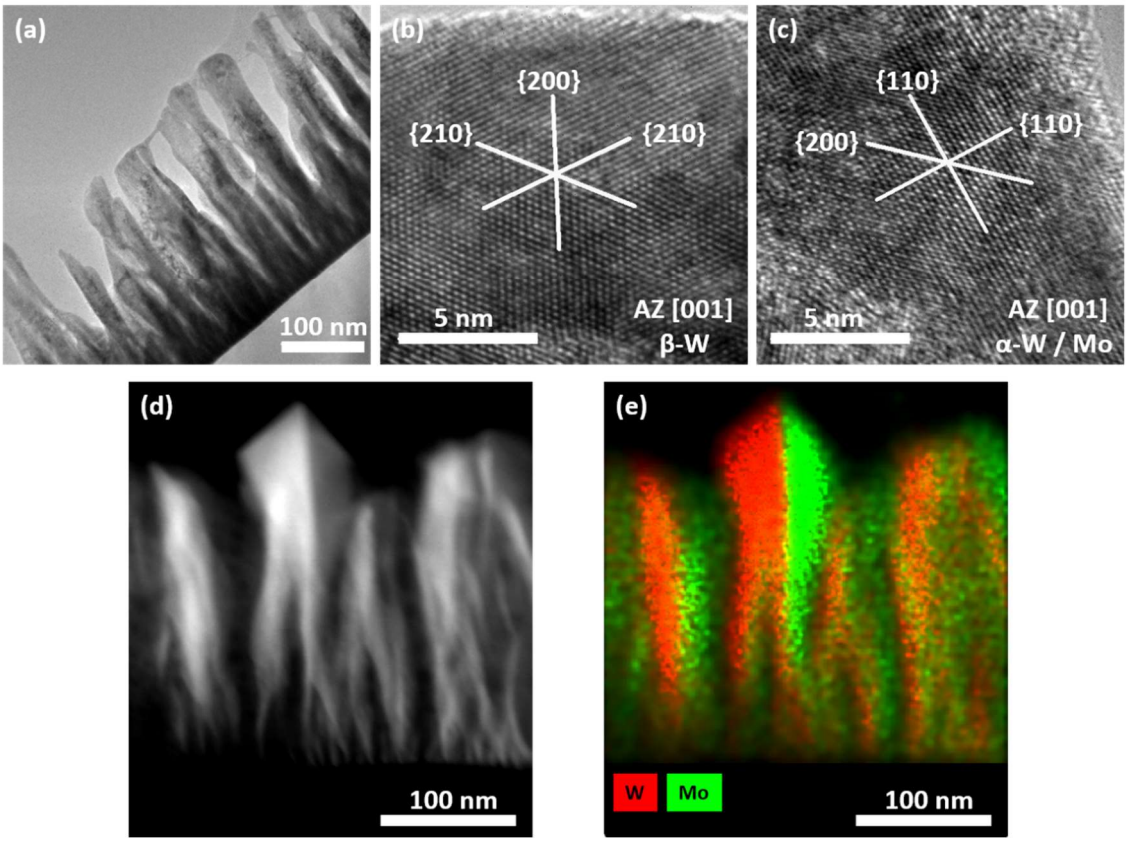
(a)
100 nm
(b)
{200}
{210}
{210}
5 nm
AZ [001]
β-W
(c)
{110}
{200}
{110}
5 nm
AZ [001]
α-W / Mo
(d)
100 nm
(e)
W
Mo
100 nm

Figure 6

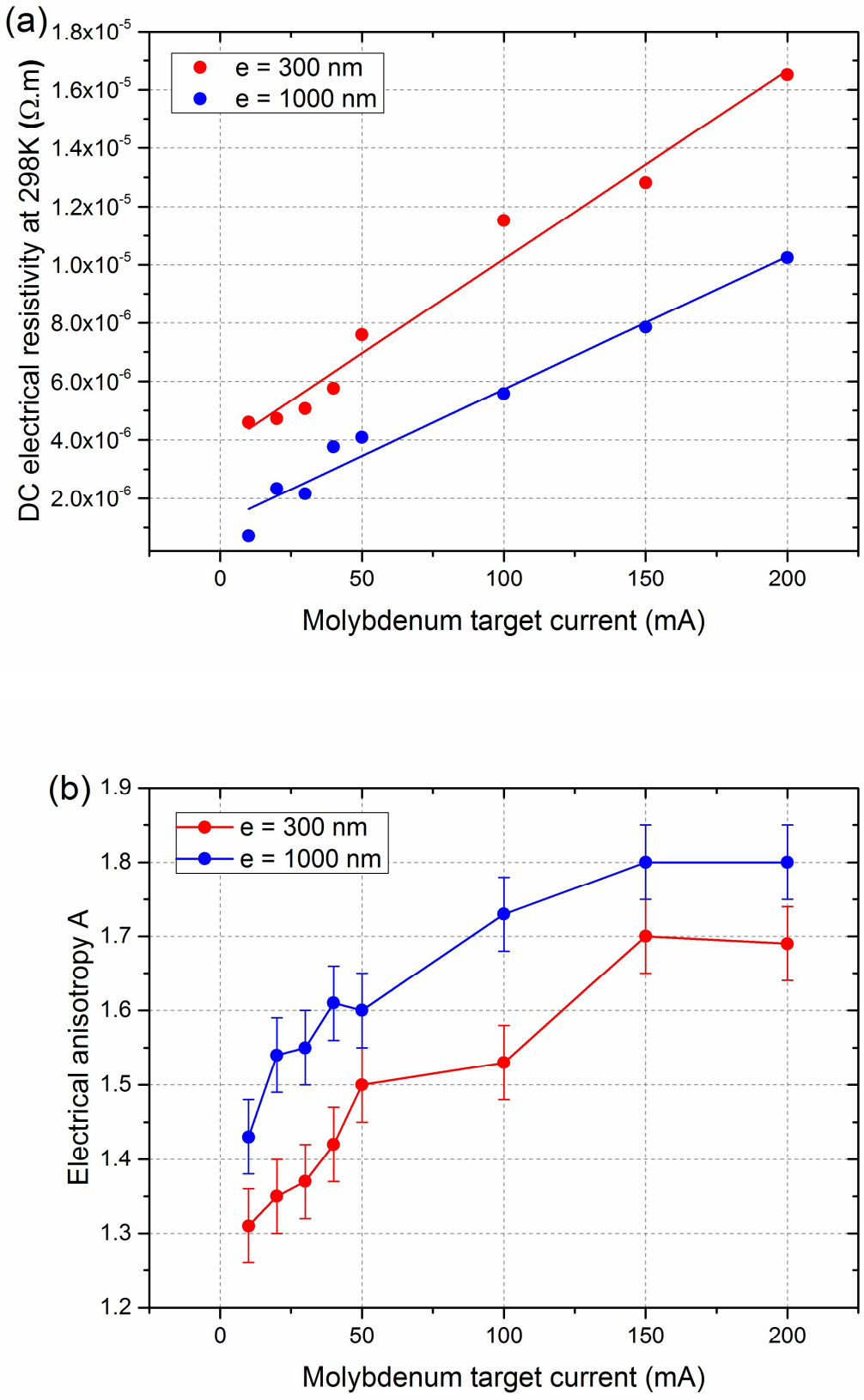
(a)
e = 300 nm
e = 1000 nm
DC electrical resistivity at 298K (Ω.m)
1.8x10-5
1.6x10-5
1.4x10-5
1.2x10-5
1.0x10-5
8.0x10-6
6.0x10-6
4.0x10-6
2.0x10-6
0
50
100
150
200
Molybdenum target current (mA)
(b)
e = 300 nm
e = 1000 nm
Electrical anisotropy A
1.9
1.8
1.7
1.6
1.5
1.4
1.3
1.2
0
50
100
150
200
Molybdenum target current (mA)

Figure 7

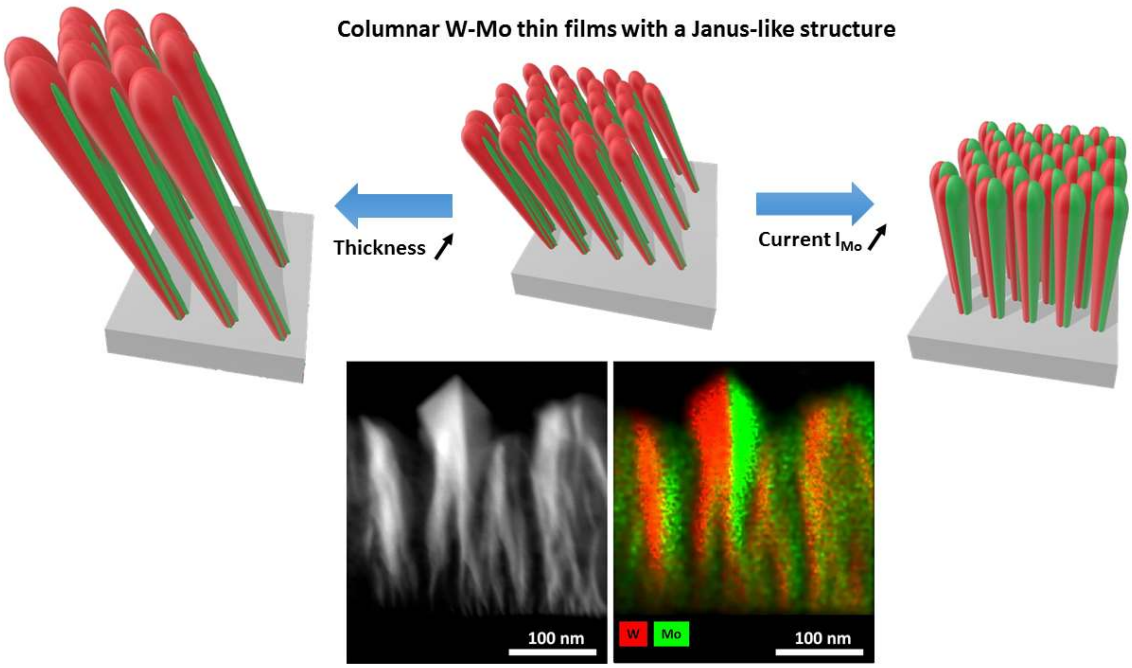

Graphical abstract